

# Modeling the Jet Kinematics of the Black Hole Microquasar XTE J1550-564: A Constraint on Spin-Orbit Alignment

James F. Steiner<sup>1</sup> and Jeffrey E. McClintock<sup>1</sup>

jsteiner@cfa.harvard.edu

## ABSTRACT

Measurements of black hole spin made using the continuum-fitting method rely on the assumption that the inclination of the black hole's spin axis to our line of sight is the same as the orbital inclination angle  $i$  of the host binary system. The X-ray and radio jet data available for the microquasar XTE J1550–564 offer a rare opportunity to test this assumption. Following the work of others, we have modeled these data and thereby determined the inclination angle  $\theta$  of the jet axis, which is presumed to be aligned with the black hole's spin axis. We find  $\theta \approx 71^\circ$  and place an upper limit on the difference between the spin and orbital inclinations of  $|\theta - i| < 12$  deg (90% confidence). Our measurement tests for misalignment along the line of sight while providing no constraint perpendicular to this plane. Our constraint on the misalignment angle supports the prediction that the spinning black hole in XTE J1550–564 has aligned itself with the orbital plane and provides support for the measurement of its spin via the continuum-fitting method. Our conclusions are based on a simple and reasonable model of a pair of symmetric jets propagating into a low density cavity whose western wall is  $\approx 20\%$  closer to XTE J1550–564 than its eastern wall.

*Subject headings:* black hole physics — stars: individual (XTE J1550–564) — X-rays: binaries

## 1. Introduction

Although it is thought that the Galaxy is host to tens of millions of stellar-mass black holes, only about 50 have been discovered (Özel et al. 2010). All of them are accretion-powered X-ray sources that are located in X-ray binary systems. Most such systems, which

---

<sup>1</sup>Harvard-Smithsonian Center for Astrophysics, 60 Garden Street, Cambridge, MA 02138.

are similar to our featured black hole binary XTE J1550–564, have short orbital periods ( $P \sim 1$  d) and are comprised of a low-mass ( $\lesssim 1 M_\odot$ ) donor star and a  $\sim 10 M_\odot$  black hole. A stream of gas from the Roche-lobe-filling star feeds into the outer part of an accretion disk that encircles the black hole. On a time scale of weeks, viscous forces in the disk cause this gas to move radially inward to the center. Within a few hundred kilometers of the black hole, the optically-thick gas reaches a temperature of  $\sim 10^7$  K and produces an X-ray luminosity that is near the Eddington limit ( $L \sim 10^{39}$  erg s $^{-1}$ ). Accretion onto the black hole is not a steady process: A typical source is luminous for only about a year, and then it fades into a quiescent state for years or decades.

XTE J1550–564 (hereafter J1550) is a much-studied Galactic black-hole transient system that was discovered on 1998 September 6 using the All-Sky Monitor (ASM) onboard the *Rossi X-ray Timing Explorer* (RXTE). Thereafter, it was observed almost daily during its entire 8-month outburst cycle using RXTE’s pointed instruments (Sobczak et al. 2000). Two weeks into outburst, the source abruptly rose fourfold in intensity and produced a brilliant 7-Crab flare. During this X-ray flare, J1550 was approximately at its Eddington limit for  $\approx 1$  day (Steiner et al. 2011). Four days later, radio observations made using the Australian Long Baseline Array (LBA) revealed relativistic ejecta moving both eastward and westward from J1550 (Hannikainen et al. 2009). The two components were observed to be separated by  $\sim 250$  mas and moving at relative speed of  $\mu_{\text{app}} \approx 65$  mas/d, equivalent to an apparent separation velocity of  $\sim 1.7c$ . Nearly two years later, *Chandra* imaging observations revealed large-scale ( $\gtrsim 20''$ ) relativistic jets undergoing deceleration (Corbel et al. 2002). This landmark discovery of a pair of ballistic X-ray jets was the first detection of its kind for a Galactic source.

By modeling an extensive collection of optical and infrared data for J1550, Orosz et al. (2011) have determined the mass of the black hole primary,  $M = 9.1 \pm 0.6 M_\odot$ , the distance to the binary,  $D = 4.38^{+0.58}_{-0.41}$  kpc, and the inclination of its orbital plane,  $i = 74.7 \pm 3.8$ . Assuming that the black hole’s spin is aligned with the orbital angular momentum, Steiner et al. (2011) have measured the spin using the continuum-fitting method to be  $a_* = 0.34^{+0.20}_{-0.28}$ , where  $a_* \equiv cJ_{\text{spin}}/GM^2$  is the black hole’s dimensionless spin parameter and  $J_{\text{spin}}$  its angular momentum. Steiner et al. also measured the spin using the independent Fe-line method and find  $a_* = 0.55^{+0.10}_{-0.15}$ ; taken together, the two measurements imply  $a_* \approx 0.5$ . The continuum-fitting method relies on a model for the thermal emission from an accretion disk (Zhang et al. 1997), while the Fe-line method relies on a model of the relativistically broadened fluorescence features emitted by the disk (Fabian et al. 1989).

For a black-hole binary system like J1550, with a low-mass companion, the ratio of the orbital angular momentum to the spin angular momentum of the black hole is given by

$$J_{\text{orb}}/J_{\text{spin}} \approx 65 a_*^{-1} \left( \frac{M}{10 M_\odot} \right)^{-4/3} \left( \frac{M_2}{M_\odot} \right) \left( \frac{P}{1 \text{ d}} \right)^{1/3}, \quad (1)$$

where  $M_2$  is the mass of the secondary star. For J1550, this ratio is  $\approx 50$ , and thus it is reasonable to expect that, given a means of interaction, the spin of the black hole will eventually come into alignment with the orbital angular momentum. The time scale for this to occur is an important question for continuum-fitting spin measurements because in applying this method one generally must assume that the two vectors are aligned.

If there is an initial misalignment between the spin and the orbital angular momenta, then Lense-Thirring precession will cause the inner X-ray-emitting portion of the disk to line up with the spin of the black hole (Bardeen & Petterson 1975). At the same time, at very large scales, the disk will align itself with the orbital plane, and the transition between these regimes will manifest as a warp in the disk. When a misalignment is present, the black hole will be torqued into alignment by the accreting matter acting with a lever arm of order the warp radius (e.g., Natarajan & Pringle 1998). Using a maximally conservative (minimum-torque) assumption, Fragos et al. (2010) concluded (based on a population synthesis study) that the spin axes of most black hole primaries will be tilted less than  $10^\circ$ . Fragos et al. assumed that the torque acts at the innermost stable circular orbit,  $R_{\text{ISCO}} < 6GM/c^2$  for  $a_* > 0$ , whereas the warp radius has been estimated to be located at  $R_w \approx 200GM/c^2$  (King et al. 2005; Lodato & Pringle 2006).

For a typical system, the time scale for accretion to torque the black hole into alignment has been estimated to be  $t_{\text{align}} \sim 10^6 - 10^8$  years (Martin et al. 2008; Maccarone 2002)<sup>1</sup>. Therefore, one expects alignment to occur early in the lifetime of an old-population transient system, such as J1550, and that most such systems will presently be well aligned.

It is obviously important to test this theoretical expectation. However, it has proved challenging to obtain a firm measurement of the degree of alignment for any black hole binary. Such a measurement requires a determination of the position angle of the binary on the plane of the sky. While this may be possible in the future for J1550, we lack the requisite orbital astrometric data for the system and are therefore limited to testing for alignment along the line of sight. Measuring the orbital inclination angle of the binary is relatively simple and is routinely done by modeling optical data (e.g., Orosz et al. 2009). In contrast, it has proved difficult to obtain reliable estimates of the inclination of the inner disk.

---

<sup>1</sup>Maccarone (2002) overestimated  $t_{\text{align}}$  as the result of a numerical error in his Eqn. 6, which implies a time scale that is 50 times longer than that implied by his Eqn. 1.

Currently, the most direct way of determining the inner-disk inclination is by modeling jet ejecta, which are presumed to be aligned with the black hole’s spin axis. For the case of symmetric ejecta, see the review by Mirabel & Rodríguez (1999). The jet ejecta that are relevant to this paper are pairs of discrete, detectable condensations of radio-emitting plasma, which we generally refer to in shorthand as “jets.”

An alternative approach to measuring the inner-disk inclination is via the same Fe-line method that is used to measure black hole spin (Reynolds & Nowak 2003). However, existing models make simplifying assumptions concerning how the ionization state of the disk varies with radius. Given that there is a degeneracy between ionization and inclination in Fe-line/reflection models for stellar-mass black holes, these inclination estimates are subject to a systematic uncertainty of unknown magnitude. Meanwhile, prospects are good that more advanced reflection models will provide robust estimates of inclination.

Based on observations of radio jets, two confirmed black hole systems, GRO J1655–40 and SAX 1819–2525, are good candidates for hosting misaligned black holes. In the case of GRO J1655–40, using a kinematic model for the jets and measurements of proper motion, Hjellming & Rupen (1995) reported a jet inclination angle of  $85^\circ$ . However, the authors give no error estimate for either the jet inclination angle or the proper motion. Furthermore, the reliability of the estimate for the jet inclination angle is called into question by the intrinsic and variable asymmetries that were observed for the opposing jets (Mirabel & Rodríguez 1999). Taking the  $85^\circ$  jet inclination angle at face value, one concludes that the jet axis and orbital vector are misaligned by  $> 15^\circ$  (Greene et al. 2001).

In the case of SAX J1819–2525, the evidence is less certain. There is only a single observation of extended radio emission (because the source faded promptly). By making the assumption that this emission was associated with a major X-ray outburst that occurred hours earlier, superluminal motion ( $\beta_{\text{app}} > 10c$ ) and a misalignment angle of  $> 50^\circ$  were inferred (Orosz et al. 2001; Hjellming et al. 2000). However, as Chaty et al. (2003) have argued, the jet may have been ejected a couple of weeks before the major outburst, in which case the Lorentz factor of the jet was modest and its inclination consistent with the inclination of the binary. This is a reasonable possibility given that the source was observed to be active at optical wavelengths for several weeks before the X-ray outburst.

Compared to the jets in these two systems and those in other Galactic microquasars, the jet ejections observed for J1550 are remarkable. They were observable for years (rather than weeks or months), and therefore their physical separation from J1550 was observed to become exceptionally large. These are possibly the largest resolved jets observed for any black hole when considering the dimensionless distance between them, i.e.,  $d/M$  (Hao & Zhang 2009, and see Heinz 2002). By this measure, the maximum 0.7 pc distance between the jet and

J1550 corresponds to 7 Mpc for a supermassive black hole of  $10^8 M_{\odot}$ .

In a previous study, Wang et al. (2003) modeled the evolution and light curve of J1550’s ballistic jets using the same model we employ, namely, an expanding jet interacting with the interstellar medium (ISM). They modeled the data for the eastern jet, attributing the X-ray emission to a reverse shock, and found that the gas density around J1550 is unusually low. Later, their work was extended by Hao & Zhang (2009) to include the western jet. Both groups focused their attention on the properties of the environment around J1550; accordingly, they adopted nominal and fixed values for jet inclination ( $50^{\circ}$  and  $68^{\circ}$ , respectively), initial Lorentz factor (3), and jet energy ( $3.6 \times 10^{44}$  erg). Both groups found evidence for the existence of a low density cavity around J1550 (modeled in more detail by Hao & Zhang), and a possible east-west asymmetry in the ambient gas.

While we follow in the footsteps of Wang et al. and Hao & Zhang, our aim is different. We are focused on the question of the alignment of the inclination angle of the black hole’s spin axis and the orbital inclination angle. Therefore, in distinction with the earlier work, we disregard the X-ray light-curve data, which are primarily useful in constraining the emission mechanisms or the electron density and magnetic fields in the jet. Rather, we concentrate on modeling the kinematics of the ballistic jets and deriving reliable values and error estimates for the kinematic parameters. The parameter of chief interest is the inclination of the black hole’s spin axis.

## 2. Data

We use archival *Chandra X-ray Observatory* data for eight observations of J1550 that were obtained using the Advanced CCD Imaging Spectrometer (ACIS) between 2000 June and 2003 October. The exposure times range from 4 – 50 ks. Pipeline processed level-2 event files<sup>2</sup> were used to produce images of the field of J1550. When detected, images of the eastern (approaching) jet yielded 16–40 counts and the western (receding) jet 100–400 counts; J1550 itself was always detected and yielded 60–3000 counts.

These same *Chandra* data were used by Hao & Zhang (2009) in their analysis of the X-ray jets. They relied on the absolute astrometric precision of *Chandra* in order to derive positions for each jet and thereby its offset from J1550. We have reduced the astrometric errors severalfold by directly measuring in each image the relative separations between J1550 and the jets.

---

<sup>2</sup>using CXC DS-7.6.10

In measuring the precise jet positions, which are given in Table 1, we smoothed each image using a  $1''$  Gaussian kernel and then determined the centroid of each jet using the DAOphot FIND routine (Stetson 1987). This procedure was used to derive initial estimates for all the jet positions. Then, 1000 Poisson random realizations of each field were produced, and the centroid measurements were repeated. In most cases, the positions for a given jet were tightly clustered about a single value, and a separation and error were derived from this distribution. However, for three observations of the eastern jet (Obs. X1, X3, and X6 in Table 1) the images are particularly faint (possibly because the emission is extended), which resulted in a broad distribution of positions. In these cases, a Gaussian-weighted mean based on the jet position angle  $\phi_j$  for each realization  $j$  was used to derive the separation between the jet and J1550. As a reference value, we used the average position angle for the jets  $\phi_{\text{PA}}$  along with its error  $\sigma_{\text{PA}}$ ,  $\phi_{\text{PA}} = 94^\circ.25 \pm 0^\circ.3$  (measured east of north). This value is consistent with those determined by Hannikainen et al. (2009) and Corbel et al. (2002) and was measured for a single frame generated by coaligning and coadding all of the X-ray images. The weights  $w_j$  were calculated according to  $\log(w_j) = -\frac{1}{2}(\phi_j - \phi_{\text{PA}})^2/\sigma_{\text{PA}}^2$ . Typically, the position errors for the eastern jet were several tenths of an arcsec, while for the brighter western jet they were  $\lesssim 0.1''$ .

In addition to the positions derived using the *Chandra* data, we include in our analysis two radio positions (Obs. R1 and R2 in Table 1). These measurements are taken from Corbel et al. (2002), who derived positions from observations obtained using the Australia Telescope Compact Array (ATCA) on 2000 June 1 and 2002 January 29. In the first observation, only the eastern jet is observed, whereas in the second, the eastern jet has faded and the western jet alone is present.

As a final constraint on our kinematic jet model, we require that the apparent separation speed of the jets at launch match the value measured using the LBA,  $65.5 \pm 13.2$  mas/d Hannikainen et al. (2009). This speed and the jet positions are the sole inputs to our principal model in Section 5. However, in Section 6, we additionally consider radio intensity measurements given by Hannikainen et al. (2009). They report 2.29 GHz flux densities taken four and six days after the X-ray flare with intensity ratios of  $S_{E1}/S_{W1} = 3.55$  and  $S_{E2}/S_{W2} = 2.40$ , respectively; we assume that these ratios are uncertain by 25%. We also adopt their measurements of the radio spectral index,  $\psi_1 = -0.43$  and  $\psi_2 = -0.21$ , taken from flux densities measured with the ACTA at 4.8 and 8.6 GHz. The spectral index measurements and corresponding LBA images, while not strictly simultaneous, were obtained within several hours of one another.

### 3. The Jet Model

The development of our kinematic jet model follows Hao & Zhang (2009) and Wang et al. (2003). The model we use has been designed to describe gamma-ray bursts, but it is applicable to a relativistic, adiabatically expanding jet. To begin, we consider a pair of symmetric jets, each launched with a kinetic energy  $E_0$  and Lorentz factor  $\Gamma_0$ . As the jets expand into their environments, they entrain material from the surrounding medium, dissipate their kinetic energy at the shock front and heat the ISM. We neglect radiative losses and assume that the jets are confined and evolve adiabatically. Following Wang et al. (2003), we assume that particles are accelerated uniformly and randomly at the shock front. Each such jet obeys the relation

$$E_0 = (\Gamma - 1)M_0c^2 + \sigma(\Gamma_{\text{sh}}^2 - 1)m_{\text{sw}}c^2, \quad (2)$$

where  $\Gamma$  is the instantaneous bulk Lorentz factor of the jet,  $M_0$  is the mass of the jet ejecta, and  $\Gamma_{\text{sh}}$  is the Lorentz factor at the shock front. The mass of the entrained material,  $m_{\text{sw}}$ , that has been swept up by the shock is approximately  $m_{\text{sw}} = \Theta^2 m_p n \pi R^3 / 3$ , where  $\Theta$  and  $R$  are respectively the jet half opening angle and the distance the jet has traveled. The numerical factor  $\sigma$  varies from  $\approx 0.35$  for ultrarelativistic shocks to  $\approx 0.73$  in the nonrelativistic limit (Wang et al. 2003; Blandford & McKee 1976). Following Huang et al. (1999), we adopt a simple numerical scaling to interpolate between the two regimes:  $\sigma = 0.73 - 0.38\beta$ , ( $\beta = \sqrt{1 - 1/\Gamma^2}$ ).

At the shock front, the jump condition relates the bulk Lorentz factor of the jet to that of the shocked gas (Blandford & McKee 1976):

$$\Gamma_{\text{sh}}^2 = \frac{(\Gamma + 1)[\hat{\gamma}(\Gamma - 1) + 1]^2}{\hat{\gamma}(2 - \hat{\gamma})(\Gamma - 1) + 2}. \quad (3)$$

The adiabatic index  $\hat{\gamma}$  varies between  $4/3$  and  $5/3$ , which are respectively its ultrarelativistic and nonrelativistic limits. We interpolate between these regimes via  $\hat{\gamma} = (4\Gamma + 1)/3\Gamma$  (Huang et al. 1999; Wang et al. 2003; Hao & Zhang 2009).

On the plane of the sky, the apparent proper motions of the approaching and receding jets,  $\mu_a$  and  $\mu_r$ , are given by

$$\mu_a = \frac{\beta c \sin\theta}{D(1 - \beta \cos\theta)}, \quad \mu_r = \frac{\beta c \sin\theta}{D(1 + \beta \cos\theta)}. \quad (4)$$

As we show in Section 5, the simple model governed by Eqn. 2 fails to fit the observations. Motivated by the results of Hao & Zhang and Wang et al., we have generalized Eqn. 2 to allow for the jets to first propagate through a low density cavity before encountering and shocking against the ISM. In the east-west direction, we allow for the cavity to differ in

size. We additionally consider the possibility of an intrinsic asymmetry in the jets. Eqn. 2 becomes:

$$\eta E_0 = (\Gamma - 1)\eta M_0 c^2 + \sigma(\Gamma_{\text{sh}}^2 - 1)m_{\text{sw}}c^2, \quad (5)$$

and the entrained mass is now

$$m_{\text{sw}} = \frac{\Theta^2 m_p n \pi}{3} \times \begin{cases} R^3, & R \leq \zeta R_{\text{cr}}, \\ (\zeta R_{\text{cr}})^3 + \delta[R^3 - (\zeta R_{\text{cr}})^3], & R > \zeta R_{\text{cr}}, \end{cases} \quad (6)$$

where  $R_{\text{cr}}$  and  $\delta$  are respectively the radius of the cavity centered on J1550 and the density jump at the cavity boundary. The ratio of the western-to-eastern cavity dimensions is given by  $\zeta$ . Similarly,  $\eta \equiv \frac{(E_0/n\Theta^2)_{\text{west}}}{(E_0/n\Theta^2)_{\text{east}}}$  parameterizes the asymmetry of the jets. In application, the asymmetry parameters  $\zeta$  and  $\eta$  are taken to be unity for the eastern jet and can vary for the western jet.

In order to obtain a model solution for a particular set of parameters, we evolve the energy equation as the jet expands (either Eqn. 2 or Eqn. 5) in 4-hour time-steps by sequentially solving for  $\Gamma(t)$  in the rest frame of J1550. At each time step, we calculate the separation between each jet and the central source by integrating  $\beta(t)$  and by calculating the projected angles  $\alpha$ :  $\alpha(t') = R(t)\sin \theta/D$ . Here,  $t' = t \mp R(t)\cos \theta/c$  is the observer's time, which takes into account the time delay between J1550's rest frame and that of the observer for whom the light-travel paths of the approaching and receding jets are respectively shortened and elongated.

Our model requires up to eight physical parameters:  $\theta$ ,  $\Gamma_0$ ,  $D$ ,  $R_{\text{cr}}$ ,  $\delta$ ,  $\eta$ ,  $\zeta$ , and lastly the “effective energy”  $\tilde{E}$  which we now define. As alluded to above, a degeneracy exists in our model between jet energy, ambient gas density, and the jet opening angle. These three quantities appear as a single and inseparable term in the kinematic equations,  $E_0/n\Theta^2$ . To make physical sense of this combined quantity, we assume that the density of the ISM is a standard  $n_{\text{ISM}} = 1 \text{ cm}^{-3}$ , so that  $n = 1/\delta \text{ cm}^{-3}$ , and adopt  $\Theta = 1^\circ$  (Kaaret et al. 2003). Predicated upon our assumed values for  $n_{\text{ISM}}$  and  $\Theta$ , the jet energy  $E_0$  is then  $E_0 = \tilde{E}$ .

Finally, we go beyond our principal, kinematic model to consider the ratio of the radio intensities of the two jets. We consider the simplest case of the ejection of a pair of identical and unimpeded condensations. When measured at equal separation from the black hole, one has

$$\frac{S_a}{S_r} = \left( \frac{1 + \beta \cos \theta}{1 - \beta \cos \theta} \right)^{3-\psi}, \quad (7)$$

where  $\psi$  is the spectral index and the subscripts  $a$  and  $r$  refer to the approaching and receding jets, which are taken to be discrete ejecta (Mirabel & Rodríguez 1999). Because the jets are observed at unequal distances from the black hole, we must adopt a model of how



jet intensity varies with time; we assume a simple power-law dependence. Then, allowing for our case of intrinsically asymmetric jets, Eqn. 7 becomes

$$\frac{S_a}{S_r} = \left[ \frac{\Gamma_r(1 + \beta_r \cos \theta)}{\Gamma_a(1 - \beta_a \cos \theta)} \right]^{3-\psi-\Delta} \eta^q, \quad (8)$$

where  $\Delta$  is a fit parameter, which for positive values describes a decay in brightness with time. The effect of jet asymmetry on the radio emission is captured by  $q$ , which can range from -1 to 1.5 depending on the source of asymmetry:  $E_0$  ( $q = -1$ ),  $n$  ( $q = 0$ ), or  $\Theta$  ( $q \in [1, 1.5]$ ).

#### 4. Markov Chain Monte Carlo

Markov Chain Monte Carlo (MCMC) is a powerful statistical technique by which random samples are drawn from a posterior distribution of arbitrary form. In our case, the posterior distribution is the probability of our model parameters, given the data. MCMC algorithms perform a “guided walk” of transitions through parameter space such that, after an initial burn-in phase, the chain directly reproduces the likelihood surface for the model. MCMC has several advantages over traditional gridded-search algorithms when the number of parameters is large. For example, the search time with MCMC scales approximately linearly with the number of parameters rather than exponentially (Martínez et al. 2009). Furthermore, the ergodic property of the Markov Chain guarantees (asymptotically) that the chain will fully explore parameter space and reach the optimum global solution.

Transitions in the chain are effected via a “jump” distribution<sup>3</sup>  $J(x^*|x_n)$  (e.g., a multivariate Gaussian) that defines a probability of selecting a candidate transition to a new state  $x^*$  given the current state  $x_n$ . The transition probability from  $x_n$  to  $x^*$  is governed by the Metropolis-Hastings algorithm (Hastings 1970) and is determined by the ratio  $r$  of probability densities

$$r = \frac{p(x^*|y)J(x_n|x^*)}{p(x_n|y)J(x^*|x_n)}, \quad (9)$$

where  $y$  refers to the data, and  $p(a|b)$  should be read in the usual way as the probability of  $a$  given  $b$ . The term  $p(x^*|y)/p(x_n|y)$  in the equation above gives the likelihood ratio of the two states, while the remaining term corrects for bias introduced by the jump-distribution

---

<sup>3</sup>We implement a particular class of the algorithm known as random-walk MCMC. In this approach, a sequence of transitions from the current parameter values are proposed and are then incrementally accepted or rejected.

density at each state. The state of the next link in the chain,  $x_{n+1}$ , is then chosen according to

$$x_{n+1} = \begin{cases} x^*, & \text{with probability } \min[r, 1], \\ x_n, & \text{otherwise.} \end{cases} \quad (10)$$

The likelihood ratio appearing in Eqn. 9 is calculated by evaluating the  $\chi^2$  for each state while taking into account the prior  $\wp$  on all of the model parameters. In this case, the priors are introduced independently so that  $\wp \equiv \prod_{k=1}^N \wp_k$ , where  $N$  is the number of parameters and  $\wp_k$  gives the prior for parameter  $k$ . Omitting additive constants, the log-likelihood for state  $x$  is

$$\log(p(x|y)) = -\frac{1}{2} [\chi^2(x) - 2 \log(\wp(x))] . \quad (11)$$

#### 4.1. MCMC in Practice

As Eqn. 11 makes apparent, the prior acts as a penalty to  $\chi^2$ , and for the special case that a prior is “flat” (i.e., independent of  $x$ ), one recovers the usual least-squares formula. It is also worth noting that because the prior only enters into the MCMC chain generation as a ratio (Eqn. 9) the scaling of the prior is arbitrary. We introduce a new term for this penalized  $\chi^2$ , namely  $\chi_\wp^2$ , such that

$$\chi_\wp^2(x) \equiv \chi^2(x) - 2 \log(\wp(x)) . \quad (12)$$

Unless stated otherwise, we choose to normalize the prior so that the penalty term ( $2 \log[\wp(x)]$ ) is zero at the best fit, i.e., at the minimum value of  $\chi_\wp^2$ .

We adopt an asymmetric Gaussian prior on the distance because it has been previously measured using optical and near-infrared photometry (see Section 1; Orosz et al. 2011). For the asymmetric terms, we adopt a log-flat prior on the difference from unity, i.e.,  $\wp_\eta \propto \min[1/\eta, \eta]$  (and likewise for  $\wp_\zeta$ ). As an example and stated differently, we consider a term implying a 10-fold asymmetry to be *a priori* one tenth as likely as one that is symmetric. We adopt flat priors on  $\theta$  and  $R_{\text{cr}}$  and flat priors on the log-values of scale parameters (i.e., the jet energy,  $\Gamma_0$  and  $\delta$ ). The priors and parameter ranges<sup>4</sup> are discussed further and illustrated in Section 5.

---

<sup>4</sup>While it is optimal to use an unbounded parameter space in performing MCMC sampling, it is also sensible to set physically meaningful constraints on the parameters (e.g.,  $\Gamma_0 > 1$ ). To achieve both objectives, we have transformed each parameter using a logit function to map a parameter  $z$  from its range  $[z_{\min}, z_{\max}]$  onto an infinite scale:  $\text{logit}(t) \equiv z_{\min} + (z_{\max} - z_{\min})/(1 + e^{-t})$  for  $-\infty < t < \infty$ .

In order to initialize the chain and the jump distribution, we make starting guesses for the model parameters and step sizes. These initial values are improved upon by running a sequence of “training” iterations. The training phase incrementally improves the jump function until its shape is a close approximation to the posterior covariance matrix, thereby greatly increasing the MCMC efficiency. The sequence becomes increasingly tuned to the likelihood surface, simultaneously refining  $\Sigma$  (the covariance estimate)<sup>5</sup> and optimizing the solution.

The training phase continued for a minimum of 15 iterations, each of which generated a trial chain with 2000 elements. Training terminated either after 25 cycles were completed or when the chain attained an acceptance fraction between 24% and 37%<sup>6</sup>.

Upon completing the training cycle, 8 chains were generated and run in parallel using the trained jump function, each to a length of 110 thousand elements. Seven of the starting positions were chosen by sampling using a dispersed covariance  $\Sigma' = 10 \Sigma$  about the final training position, and the eighth was started directly from the end location reached by the training sequence. The initial 10,000 elements of each chain were rejected as the “burn-in” phase during which the chains relax toward a stationary distribution. Our final results are based on a total of  $8 \times 10^5$  MCMC samples. Convergence of the MCMC run is determined using the criterion of Gelman & Rubin (1992),  $\hat{R}$ . The closeness of this criterion to unity is the measure of convergence.

In Figure 1, we plot a trace of our parallel runs over time for inclination in our adopted model (see Section 5). In the bottom panel, we show the Gelman & Rubin convergence diagnostic of the chain over time. Typically, a chain is considered converged if  $\hat{R} \leq 1.1$ , or 1.2 (see, e.g., Verde et al. 2003)<sup>7</sup>. For  $\theta$ , our parameter of interest, we obtain  $\hat{R} < 1.01$ .

---

<sup>5</sup> $\Sigma$  is calculated from the chain positions and is used to define the jump function for each sequence. The jump function is taken to be a  $t$ -distribution with 4 degrees of freedom that is symmetric about the present position.

<sup>6</sup>The target acceptance fraction was set at  $\approx 32\%$ . The optimal value ranges from  $\approx 23\%$  for an infinite-dimensional problem to  $\approx 45\%$  for a univariate problem (Gelman et al. 1996). Each run produced an acceptance fraction of at least 20%

<sup>7</sup>Larger values of  $\hat{R}$  suggest that either the parameter space is insufficiently sampled or that the chains are not fully evolved.

Table 1. Relative Jet Positions

Obs.	$\Delta t'^a$ (d)	Eastern Offset (arcsec)	Western Offset (arcsec)
R1	620.5	$21.9 \pm 0.3^b$	...
X1	628.5	$21.5 \pm 0.5$	...
X2	701.4	$22.7 \pm 0.2$	...
X3	722.2	$23.7 \pm 0.5$	...
R2	1227.5	...	$22.6 \pm 0.3^b$
X4	1268.8	$28.5 \pm 0.2$	$22.78 \pm 0.05$
X5	1368.5	...	$23.19 \pm 0.07$
X6	1466.0	$29.6 \pm 0.6$	$23.44 \pm 0.10$
X7	1591.3	...	$23.76 \pm 0.10$
X8	1859.6	...	$24.4 \pm 0.2$

<sup>a</sup>Time since the jets were launched: MJD - 51076.

<sup>b</sup>ACTA position from Corbel et al. (2002).

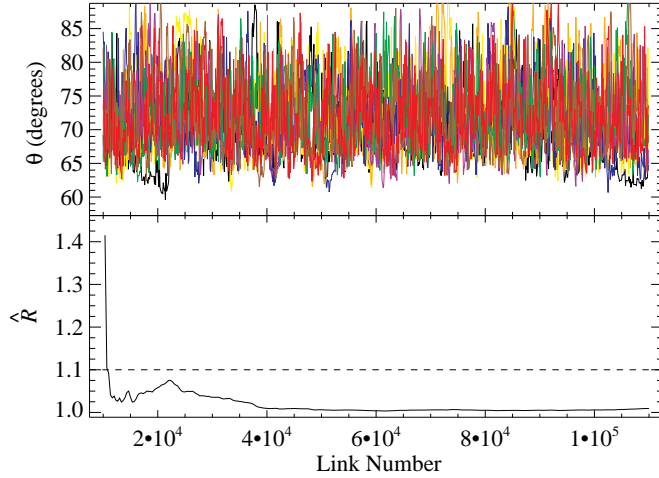


Fig. 1.— *top*: The trace of  $\theta$  for Model AC of Section 5. Eight parallel chains are used; for each, the initial  $10^4$  elements are generated during the burn-in phase and discarded from the analysis. *bottom*: The convergence of the chain over time. The chains reach convergence quickly, which is indicative of efficient sampling.

## 5. Results

In this section we consider three symmetric-jet models, including our adopted model. For these models, and for the additional models discussed in the following section, we assume that the jets were launched at the time of J1550’s giant X-ray flare (Section 1).

### 5.1. Two Preliminary Models

We first consider and rule out two simple models. For the simpler of these, which we refer to as Model S1, the jets are symmetric and propagate through a uniform medium (Eqn. 2; i.e.,  $\eta = \zeta = \delta = 1$  and  $R_{\text{cr}} = 0$ ). The strong deceleration of the jets at late times is not accommodated by this model, and the best fit achieved is unacceptable,  $\chi^2_{\phi}/\nu = 68$ . For Model S2, we introduce a symmetric cavity centered on J1550 with  $\delta$  and  $R_{\text{cr}}$  as free fit parameters. The fit is significantly improved,  $\chi^2_{\phi}/\nu = 42$ , but it is still far from acceptable. The results for both models are given in Table 2.

### 5.2. Our Adopted Model

We now consider our primary model – an extension of Model S2 that allows the source to be positioned off-center in the cavity. This asymmetric cavity model (Model AC) is obtained by freeing the fit parameter  $\zeta$  (while leaving  $\eta$  fixed at unity; see Eqn. 5). As illustrated in Figure 2, for a modest (22%) degree of asymmetry, this model produces a successful fit to the data with  $\chi^2_{\phi}/\nu = 1.44$ . Results are given in Table 2 and marginal distributions from the MCMC run are shown for each parameter in Figure 3.

The eastern and western cavity walls are located respectively at 0.6 pc and 0.5 pc from the black hole and the density contrast at the boundary of the cavity is  $\sim 100$ . The gas density within the cavity is much lower than that of the ISM. This must be the case in order for the jets to have passed through without sweeping up enough mass to halt their expansion. Motion within the cavity lasted for  $\approx 1.5$  years (in the frame of J1550), until the receding western jet impacted the dense ISM at its cavity wall and abruptly began decelerating in advance of its eastern counterpart (see Fig. 2).

The total energy for both jets is an impressive  $E_{\text{tot}} \approx 10^{46} \text{ erg } \frac{n_{\text{ISM}}}{1 \text{ cm}^{-3}} \left( \frac{\Theta}{1 \text{ deg}} \right)^2$ . At launch, the Lorentz factor of the jets is constrained to be  $\Gamma_0 > 1.6$  (99.7% confidence). However, the data provide no upper limit on  $\Gamma$ , as implied by Figure 3, which shows that for large values of  $\Gamma$  the distribution closely tracks the prior. Likewise, the data only weakly constrain J1550’s

distance. However, the remaining five parameters are well determined by the data and are quite independent of their priors (Fig. 3). For the key parameter, the jet inclination angle, we obtain  $\theta \approx 71^\circ$  ( $64^\circ < \theta < 83^\circ$  at 90% confidence) and find only moderate correlations with the other fit parameters. The strongest of these correlations are with  $\zeta$  and with  $R_{\text{cr}}$ , which are illustrated in Figure 4.

### 5.3. Constraining Spin-Orbit Alignment

We now use Model AC and the results of our MCMC analysis to examine the relationship between the spin axis of the black hole (the same as that of the jet; see Section 1), and the orbital angular momentum vector. We assume that the inclination of the orbital plane  $i$  is Gaussian distributed:  $i = 74.7 \pm 3.8$  (Orosz et al. 2011).

Our constraints on the locations of both axes are illustrated in Figure 5, which was derived using one million Monte-Carlo draws to represent each axis. This figure shows how readily our results are able to falsify the alignment hypothesis, even though we lack a measurement of the position angle of the orbital plane. Specifically, (1) over 80% of the sky, we are able to rule out the possibility that the spin and orbital axes are aligned<sup>8</sup>; and (2) the probability by random chance that the inclination angles agree so closely (see Fig. 6) is less than 10%.

Because the continuum-fitting method depends only on inclination angle (and not position angle), and because the difference between the inclination  $\theta$  of the spin/jet axis and the inclination  $i$  of the orbital plane is of critical importance in measuring the spin of J1550, we now use Model AC to determine  $\theta - i$ . Our results are shown in Figure 6 where it is obvious that there is no evidence for any misalignment along the line of sight. That is, our results are consistent with  $\theta = i$ . We place upper limits on the absolute difference between orbital and spin inclinations of  $8^\circ$  and  $12^\circ$  at the 68% and 90% levels of confidence, respectively.

Given the  $< 10\%$  a priori chance that the inclination angles agree as closely as measured, our results provide support for the hypothesis that the two axes are aligned. However, without knowledge of the position angle of the binary axis (which can lie anywhere along the grey band in Fig. 5), we cannot conclude whether they are, in fact, aligned.

---

<sup>8</sup>at 90% confidence

Table 2. Kinematic Model Settings and Fit Results

Parameter	Range	Prior Shape <sup>a</sup>	Model S1	Model S2	Model AC
$\theta$ (degrees)	0 – 89.99	F	$53.9 \pm 0.7$	$58.16 \pm 1.7$	$70.8^{+7.3}_{-4.5}$
$\Gamma_0$	1 – 1000	LF	$210^{+390}_{-160}$	$50^{+320}_{-43}$	$36^{+300}_{-32}$
$\tilde{E}^b$ ( $10^{45}$ erg)	$10^{-10} - 10^{10}$	LF	$91.8^{+9.6}_{-6.7}$	$74^{+18}_{-14}$	$5.9^{+3.6}_{-2.3}$
$D$ (kpc)	3 – 7 <sup>c</sup>	$N(4.38^{+0.58}_{-0.41})$	$3.07 \pm 0.06$	$4.30^{+0.29}_{-0.23}$	$4.48^{+0.43}_{-0.34}$
$R_{\text{cr}}$ (pc)	0 – 5	LF	...	$0.46 \pm 0.03$	$0.63 \pm 0.06$
$\delta$	$0.1 - 10^4$	LF	...	$940^{+4900}_{-790}$	$104^{+70}_{-34}$
$\zeta$	$10^{-2} - 10^2$	LF ( $\max[\zeta, \zeta^{-1}]$ )	...	...	$0.78 \pm 0.03$
$\min(\chi^2_{\text{g}}/\nu)$	...	...	67.93 (543.4/8)	41.59 (249.6/6)	1.44 (7.21/5)
$\min(\chi^2/\nu)$	...	...	67.61	40.94	1.22

Note. — The values quoted are the median parameter and symmetric 68% confidence interval ( $1\sigma$  equivalent) derived from the MCMC run (as opposed to the single best-fit values).

<sup>a</sup>F is flat, LF is log-flat, and N is a normal distribution.

<sup>b</sup>Assumes  $n_{\text{ISM}} = 1 \text{ cm}^{-3}$  and  $\Theta = 1^\circ$ .

<sup>c</sup>The lower bound on distance is taken from Hannikainen et al. (2009) and the upper bound is derived using  $D \leq \frac{c}{\sqrt{\mu_a \mu_r}}$  (Mirabel & Rodríguez 1999).

## 6. Radio Intensities and Asymmetric-Jet Models

We now consider the radio intensity measurements discussed in Section 2 in order (1) to identify any intrinsic asymmetry in the jets and (2) to check the consistency of our kinematic model. In doing this, we are motivated by observations of the microquasar GRO J1655–40, which in 1994 displayed multiple ejection events, each of which expanded and decayed on a time scale of a few days. The approaching and receding jets were found to be intrinsically asymmetric; additionally, the sense of the asymmetry changed from event to event (Hjellming & Rupen 1995; Mirabel & Rodríguez 1999).

Before introducing intrinsic jet asymmetry into the model, we first proceed by extending Model AC to create Model RAC. This latter model retains the traits of Model AC but now incorporates Eqn. 8 and uses the additional free parameter  $\Delta$  to model the radio data. The data set for Model RAC is likewise extended and includes its two radio intensity measurements (Section 2; Hannikainen et al. 2009). Re-fitting the data using Model RAC and comparing with the results obtained for Model AC, we find a slight ( $2^\circ$ ) increase in the jet angle and similar small changes in the other parameters (Table 3). The fit is good,  $\chi^2_\phi/\nu = 1.44$ , and  $\Delta$ , the decay rate of the jet emission, is positive and in the range  $\approx 1 - 5$ .

We now examine intrinsic jet asymmetry, and introduce Model RAJ, a model that considers both kinematics and radio emission. In this case, the cavity is presumed to be symmetric, while the energy term ( $E_0/n\Theta^2$ ) is allowed to vary between the eastern and western jets. Specifically, we set  $\zeta = 1$ , free  $\eta$ , and introduce the parameter  $q$ , which characterizes the type of asymmetry in the jets (Eqn. 8). The fit results for Models RAC and RAJ are shown in Table 3. Model RAJ returns a significantly larger jet inclination angle than Model RAC,  $\theta \approx 82^\circ$ , and it implies a large difference between the eastern and western jets,  $\eta^{-1} \sim 15$ . Because  $q \approx 0$ , for this model the gross asymmetry can be attributed to an east-west difference in the gas density (rather than an asymmetry in the energies or opening angles of the jets; see Section 3).

To assess the performance of Model RAC relative to Model RAJ, we exploit the similarities in the way these models are structured. In particular, their respective priors have identical form. Therefore, because we attribute equal likelihood to either type of asymmetry, we can apply the penalty normalization from Model RAC to Model RAJ. This yields the goodness-of-fit results shown in Table 3. Model RAJ is effectively ruled out:  $\min(\chi^2_{\phi,\text{RAJ}}) - \min(\chi^2_{\phi,\text{RAC}}) = 8.2$ .

We now test the strength of this result by considering a kinematic-only variant of this asymmetric-jet model, Model AJ, which ignores the radio intensity data. Model AJ has the virtue that it can be directly compared with our primary model, Model AC, because



both models have the same number of parameters (seven) and their priors are identically structured. As in the comparison above, we apply the penalty normalization of Model AC (Section 5) to Model AJ. The fit results for the two models are given respectively in Tables 2 and 3. Based on the substantial difference in  $\chi^2_{\phi}$ ,  $\min(\chi^2_{\phi,AJ}) - \min(\chi^2_{\phi,AC}) = 7.5$ , and the even larger difference obtained when the radio-intensity data are included, we conclude that the asymmetric cavity model is favored over the asymmetric jet model at the 99% level of confidence.

Unlike the manifestly asymmetric jets of GRO J1655–40, the available evidence indicates that the jets of J1550 are likely intrinsically symmetric: Model AC is favored over Model AJ, and Model RAJ implies an implausibly large (factor of 15) difference in the density of the ISM from west to east.

In comparison with Model AJ or RAJ, our adopted Model AC gives a reasonable and satisfying description of J1550 as a system comprised of intrinsically symmetric jets propagating through an evacuated cavity with eastern and western walls located out at 0.6 pc and 0.5 pc, respectively.

## 7. Discussion

If we assume that the jets were produced continuously over the day-long Eddington-limited X-ray flare (Steiner et al. 2011), then the nominal total jet energy of  $\approx 10^{46}$  erg implies that a significant fraction of the mass accreted onto J1550 during the flare was directly used to fuel the jets. Roughly, the initial mass in the jets was then  $\sim 10^{24}$  g and the matter was accelerated to  $\Gamma_0 \sim 10$ .

We note that the moderate asymmetry we find (with the western cavity  $\approx 20\%$  smaller in radius than the eastern) is opposite in sense from the asymmetry determined by Hao & Zhang (2009). We attribute this difference to several factors: Hao & Zhang simply adopted reasonable, ad-hoc values for several key parameters ( $\theta$ ,  $\tilde{E}$ , and  $\Gamma_0$ ), and they found a high degree of asymmetry with  $\eta^{-1} \approx 30$  and  $\zeta = 1.4$ . (We note that this particular pair of values of  $\eta$  and  $\zeta$  allowed a reasonable fit to be achieved to their data set.) By improving the quality and quantity of the astrometric data, we were able to determine that just one asymmetry parameter is required to explain the data, and that the resultant asymmetry is less extreme.

Based on results obtained for the sub-pc scale ( $\lesssim 0.1$  pc) jets of GRS 1915+105 and GRO J1655–40, Heinz (2002) has proposed that black hole microquasars preferentially inhabit environments that are under-dense compared to their AGN counterparts. Heinz offers several explanations, notably that microquasars may produce self-encasing low density bub-

Table 3. Additional Model Results

Parameter	Model AJ	Model RAC	Model RAJ
$\theta$ (degrees)	$86.2^{+2.4}_{-3.1}$	$72.8^{+7.4}_{-5.4}$	$81.9^{+5.1}_{-6.8}$
$\Gamma_0$	$22^{+270}_{-19}$	$37^{+390}_{-33}$	$1.41^{+0.33}_{-0.14}$
$\tilde{E}^a$ ( $10^{45}$ erg)	$213^{+83}_{-65}$	$6.1^{+3.8}_{-2.3}$	$80^{+30}_{-34}$
$D$ (kpc)	$4.83 \pm 0.36$	$4.49^{+0.43}_{-0.35}$	$3.57^{+0.50}_{-0.44}$
$R_{\text{cr}}$ (pc)	$0.46 \pm 0.05$	$0.63 \pm 0.06$	$0.35^{+0.04}_{-0.05}$
$\delta$	$510^{+1700}_{-410}$	$98^{+57}_{-30}$	$740^{+3300}_{-590}$
$\zeta$	...	$0.78 \pm 0.03$	...
$\eta^b$	$0.065 \pm 0.014$	...	$0.068^{+0.016}_{-0.013}$
$\Delta^c$	...	$1.9^{+3.2}_{-1.1}$	$1.8^{+5.3}_{-6.5}$
$q^d$	...	...	$-0.28^{+0.52}_{-0.35}$
$\min(\chi^2_{\phi}/\nu)$	$2.95$ (14.74/5) <sup>c</sup>	$1.44$ (8.63/6)	$3.36$ (16.81/5) <sup>c</sup>
$\min(\chi^2/\nu)$	1.11	1.11	1.31

Note. — The values quoted are the median parameter and symmetric 68% confidence interval ( $1\sigma$  equivalent) derived from the MCMC run.

<sup>a</sup>Assumes  $n_{\text{ISM}} = 1 \text{ cm}^{-3}$  and  $\Theta = 1^\circ$ .

<sup>b</sup>The form of the prior for  $\zeta$  and  $\eta$  are identical (see Table 2).

<sup>c</sup>A flat prior is used for both  $\Delta$  and  $q$ . The former is allowed to take values between  $[-10, 10]$  and the latter is constrained to the range  $[-1, 1.5]$ .

<sup>d</sup>The penalty normalization for Model AJ is taken from Model AC; likewise that for Model RAJ is from Model RAC.

bles either as a remnant of the birthing supernova explosion, or via persistent kinetic outflows from the compact source.

The enthalpy of the low density cavity in J1550,  $\sim 10^{40} - 10^{42}$  erg, is likely maintained by the steady (or quasi-steady) AU-scale jets known to be present in the hard or quiescent state of black hole binaries (Remillard & McClintock 2006; Gallo et al. 2006). The  $\sim 20\%$  measured asymmetry in the east-west extent of the cavity is unlikely to be a result of a high proper motion of the binary because this would require an extreme velocity  $\sim 0.1c$ . Rather, this asymmetry is easily explained as arising from a moderate 20% variation in the density of the ISM across the pc-scale region spanned by the jets. This supposition is quite plausible, given that J1550 is located only  $\sim 140$  pc from the Galactic plane.

One interesting feature of our best-fitting model is shown in Figure 2: The onset of X-ray emission for the western jet is first observed after the jet has reached the outer wall of the cavity, whereas for the eastern jet it occurs well before reaching the outer wall. Although there is not enough data to draw a firm conclusion, this difference in behavior suggests that our model oversimplifies by describing a succession of low-grade density jumps (from previous episodes of jet activity) as one single jump at  $R_{\text{cr}}$ . Alternatively, perhaps one or several dense filaments of gas breached the eastern cavity walls, causing X-ray brightening at the shock front, but without contributing appreciable mass.

We close our discussion by noting again that our lack of knowledge of the position angle of the binary restricts us to testing for spin-orbit alignment along the line of sight. The test we have performed nevertheless provides important support for the continuum-fitting measurement of J1550’s spin, which used the orbital inclination angle as a proxy for the inclination of the black-hole spin axis (Steiner et al. 2011). For the case of J1550, we have shown that these two inclination angles are consistent within several degrees.

## 8. Conclusions

Building on earlier work by Hao & Zhang (2009) and Wang et al. (2003), we have used *Chandra* and radio imaging data to model the ballistic motion of the jets of J1550. We take the time of J1550’s giant X-ray flare, which was promptly accompanied by the ejection of small-scale ( $\sim 1000$  AU) relativistic radio jets, as the launch date of the large-scale ballistic jets. Using our MCMC code and a kinematic model of the jets, we find that J1550 is enclosed in a pc-scale cavity that is moderately asymmetric, and that the jets are inclined by between  $64^\circ$  and  $83^\circ$  to our line of sight (90% confidence). These impulsive jets are extremely energetic, having been launched with a total energy of  $\sim 10^{46}$  erg  $\frac{n_{\text{ISM}}}{1\text{cm}^{-3}} \left( \frac{\Theta}{1\text{deg}} \right)^2$ .

By comparing our derived inclination angle for the spin axis of the black hole (taken to be the jet inclination angle) to the orbital inclination angle, we arrived at our primary result: We find no evidence for misalignment in our comparison of orbital and jet inclinations, and we conclude that the spin and orbital inclinations differ by  $< 12$  degrees (90% confidence). This result has a likelihood of less than 10% of occurring by chance.

Theory predicts that accretion torques acting over time will have brought most black holes into alignment with the orbital plane of their binary hosts. This prediction underpins the continuum-fitting method. In the case of J1550, our results provide support for such alignment and for the measured spin of its black hole primary.

JFS was supported by the Smithsonian Institution Endowment Funds and JEM acknowledges support from NASA grant NNX11AD08G. We thank Bob Penna, Sasha Tchekovskoy, and Ramesh Narayan for constructive ideas which helped shaped the direction of this work, and both Joey Neilsen and Lijun Gou for their comments on the manuscript. We thank an anonymous referee for helpful feedback which has improved this paper. The MCMC analyses were run using the Odyssey cluster supported by the FAS Science Division Research Computing Group at Harvard University.

## REFERENCES

- Bardeen, J. M., & Petterson, J. A. 1975, *ApJ*, 195, L65
- Blandford, R. D., & McKee, C. F. 1976, *Physics of Fluids*, 19, 1130
- Chaty, S., Charles, P. A., Martí, J., Mirabel, I. F., Rodríguez, L. F., & Shahbaz, T. 2003, *MNRAS*, 343, 169
- Corbel, S., Fender, R. P., Tzioumis, A. K., Tomsick, J. A., Orosz, J. A., Miller, J. M., Wijnands, R., & Kaaret, P. 2002, *Science*, 298, 196
- Fabian, A. C., Rees, M. J., Stella, L., & White, N. E. 1989, *MNRAS*, 238, 729
- Fragos, T., Tremmel, M., Rantsiou, E., & Belczynski, K. 2010, *ApJ*, 719, L79
- Gallo, E., Fender, R. P., Miller-Jones, J. C. A., Merloni, A., Jonker, P. G., Heinz, S., Maccarone, T. J., & van der Klis, M. 2006, *MNRAS*, 370, 1351
- Gelman, A., Roberts, G., & Gilks, W. 1996, in *Bayesian Statistics*, ed. J. M. Bernardo et al., Vol. 5 (OUP), 599

- Gelman, A., & Rubin, D. 1992, *Statistical Science*, 7, 457
- Greene, J., Bailyn, C. D., & Orosz, J. A. 2001, *ApJ*, 554, 1290
- Hannikainen, D. C., et al. 2009, *MNRAS*, 397, 569
- Hao, J. F., & Zhang, S. N. 2009, *ApJ*, 702, 1648
- Hastings, W. 1970, *Biometrika*, 97
- Heinz, S. 2002, *A&A*, 388, L40
- Hjellming, R. M., & Rupen, M. P. 1995, *Nature*, 375, 464
- Hjellming, R. M., et al. 2000, *ApJ*, 544, 977
- Huang, Y. F., Dai, Z. G., & Lu, T. 1999, *MNRAS*, 309, 513
- Kaaret, P., Corbel, S., Tomsick, J. A., Fender, R., Miller, J. M., Orosz, J. A., Tzioumis, A. K., & Wijnands, R. 2003, *ApJ*, 582, 945
- King, A. R., Lubow, S. H., Ogilvie, G. I., & Pringle, J. E. 2005, *MNRAS*, 363, 49
- Lodato, G., & Pringle, J. E. 2006, *MNRAS*, 368, 1196
- Maccarone, T. J. 2002, *MNRAS*, 336, 1371
- Martin, R. G., Tout, C. A., & Pringle, J. E. 2008, *MNRAS*, 387, 188
- Martínez, V. J., Saar, E., Martínez-González, E., & Pons-Bordería, M.-J., eds. 2009, *Lecture Notes in Physics*, Berlin Springer Verlag, Vol. 665, *Data Analysis in Cosmology*
- Mirabel, I. F., & Rodríguez, L. F. 1999, *ARA&A*, 37, 409
- Natarajan, P., & Pringle, J. E. 1998, *ApJ*, 506, L97
- Orosz, J. A., et al. 2001, *ApJ*, 555, 489
- . 2009, *ApJ*, 697, 573
- Orosz, J. A., Steiner, J. F., McClintock, J. E., Torres, M. A. P., Remillard, R. A., Bailyn, C. D., & Miller, J. M. 2011, *ApJ*, 730, 75
- Özel, F., Psaltis, D., Narayan, R., & McClintock, J. E. 2010, *ApJ*, 725, 1918
- Remillard, R. A., & McClintock, J. E. 2006, *ARA&A*, 44, 49

- Reynolds, C. S., & Nowak, M. A. 2003, *Phys. Rep.*, 377, 389
- Sobczak, G. J., McClintock, J. E., Remillard, R. A., Cui, W., Levine, A. M., Morgan, E. H., Orosz, J. A., & Bailyn, C. D. 2000, *ApJ*, 544, 993
- Steiner, J. F., et al. 2011, *MNRAS*, 416, 941
- Stetson, P. B. 1987, *PASP*, 99, 191
- Verde, L., et al. 2003, *ApJS*, 148, 195
- Wang, X. Y., Dai, Z. G., & Lu, T. 2003, *ApJ*, 592, 347
- Zhang, S. N., Cui, W., & Chen, W. 1997, *ApJ*, 482, L155

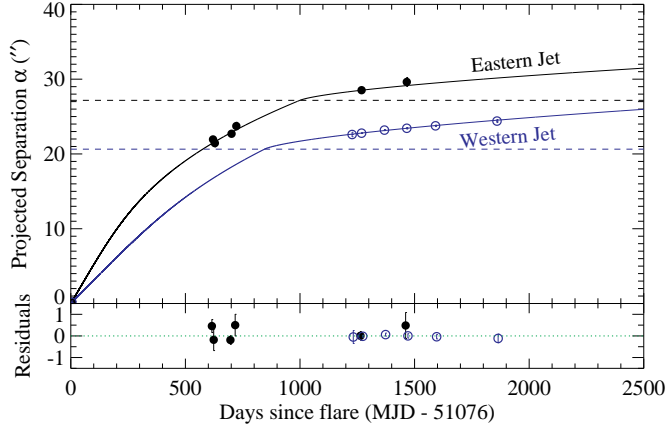


Fig. 2.— The best-fitting model and fit residuals for the eastern jet (filled circles) and western jet (open circles). The cavity locations are marked by dashed horizontal lines, which indicate that the western wall (for the receding jet) is closer to the black hole than the eastern wall. For clarity, residuals for the coincidentally detected eastern and western jets are shown slightly offset in time. In the top panel, the error bars are smaller than the symbols.

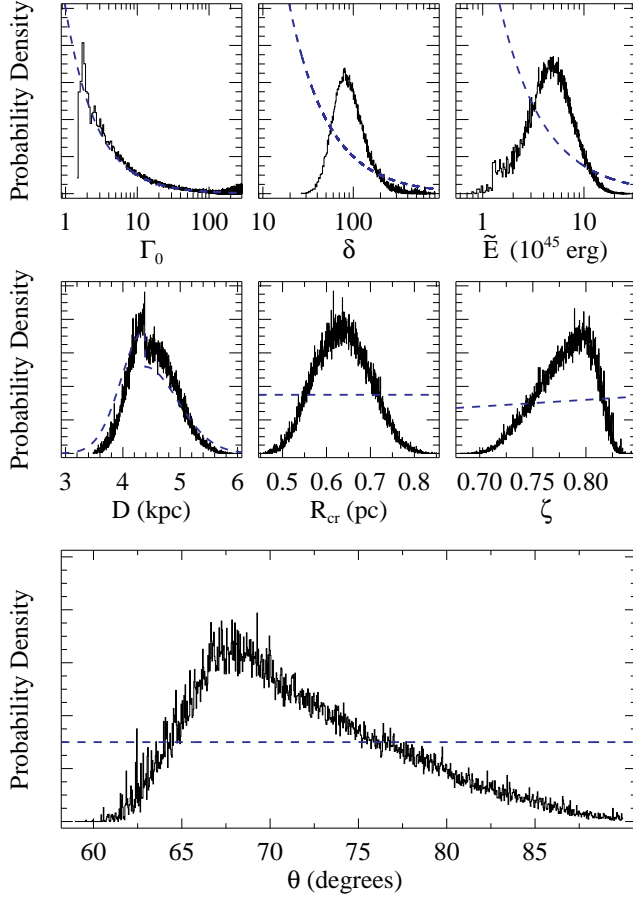


Fig. 3.— MCMC results for Model AC. Probability densities are shown for each parameter on an arbitrary scale and have been obtained by marginalizing over all other parameters. An overlay for each prior shape is drawn as a dashed line. Note that the only two parameters which closely track the prior function are the system distance and  $\Gamma_0$  (at high values only). Otherwise, the prior contributes minimally to the parameter distribution.



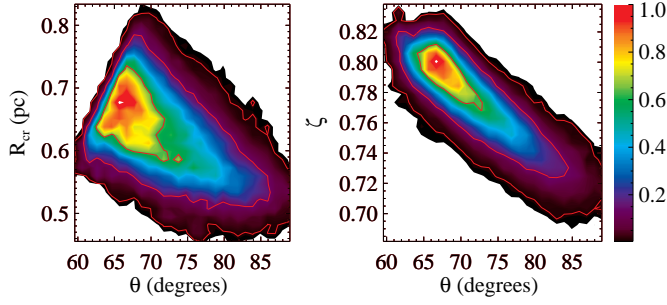


Fig. 4.— Shown for Model AC are the MCMC density contours for the two parameters that correlate most strongly with inclination: cavity size  $R_{\text{cr}}$  and the cavity asymmetry parameter  $\zeta$ . The densities are calculated by marginalizing over all unshown parameters. Red contours mark the 68%, 95%, and 99.7% confidence regions about the most likely value, which is normalized to a density of unity. The central value of  $\theta$  changes from  $70^\circ$  to  $80^\circ$  as  $R_{\text{cr}}$  varies from 0.65 pc to 0.58 pc, and as  $\zeta$  decreases from 0.78 to 0.74.

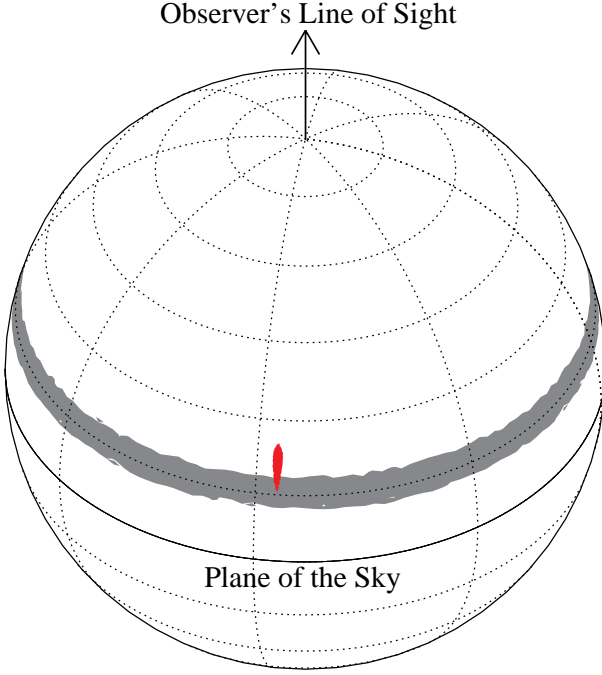


Fig. 5.— The celestial sphere centered about J1550 with the observer situated along the pole. The angular momentum of the orbital plane is constrained to lie along the grey band (drawn with  $1\sigma$  width), and the spin angular momentum axis derived from the jets is overlaid in red ( $1\sigma$  about the most likely value). The position angle is completely unbounded for the orbital angular momentum, whereas the jets provide a tight constraint on the position angle of the black hole’s spin axis (Section 2). In fact, the uncertainty in the position angle of the jets is so small ( $\pm 0.3$  deg) that for purposes of illustration it has been tripled to make it visible in this figure.

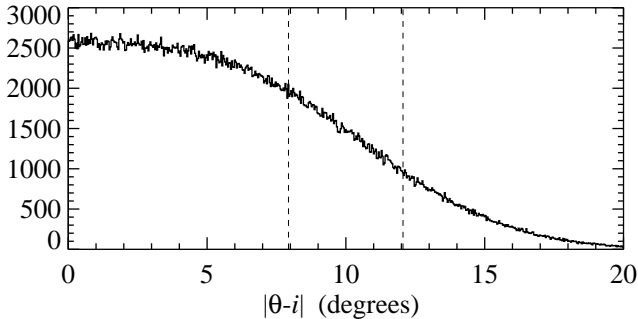


Fig. 6.— The difference in orbital and jet inclination angles derived from the MCMC run of Model AC. The results show no sign of a misalignment along the line of sight; 68% and 90% upper limits on the difference between inclinations are  $8^\circ$  and  $12^\circ$ , respectively.